Microstructure Observations of Turbulent Mixing in a Partially Mixed Estuary. Part II: Salt Flux and Stress

HARTMUT PETERS

Rosenstiel School of Marine and Atmospheric Science, University of Miami, Miami, Florida

REINOUD BOKHORST

Getronics Business Solutions, Nieuwegein, Netherlands

(Manuscript received 21 June 1999, in final form 24 July 2000)

ABSTRACT

Turbulent mixing in the water column was observed with a microstructure profiler in the Hudson River estuary during two cruises in summer and fall 1995. The focus is on the estimation of turbulent salt flux and turbulent stress from measured viscous dissipation rates (ε), and on the tidal and fortnightly variability of these fluxes. In estimating eddy viscosity (K_m) and eddy diffusivity (K_ρ), the authors follow measurement/modeling techniques of Busch and Osborn, while prescribing a variable flux Richardson number (R_f) dependent upon the gradient Richardson number (Ri). It is argued that a steady-state production–dissipation balance holds in the turbulent kinetic energy budget.

All turbulence characteristics varied strongly over semidiurnal tidal cycles and over the fortnightly cycle. Subject to complications arising from nontidal flows, the ''strongest'' mixing occurred during flood on neap tides, and during ebb on spring tides. In the lower part of the water column during floods and spring ebb K_m and K_ρ reached maxima of 1–5 ($\times 10^{-2}$ m^2 s^{-1}) and decreased roughly exponentially with increasing height by 1–3 decades. The smallest eddy coefficients occurred in the halocline during neap tide with $K_m \approx 10^{-4}$ m^2 s^{-1} and $K_\rho \approx 10^{-5}$ m^2 s^{-1}. Mostly, the internal turbulent stress (τ_y) was close to 0 in the upper third of the water column and approached the bottom shear stress with decreasing height. Neap ebb had small $|\tau_y|$ even close to the bottom in response to stable stratification. During spring ebb, in contrast, τ_y decayed approximately linearly from the bottom shear stress to 0 at the surface. The largest turbulent salt flux (J_s) of 8–10 ($\times 10^{-4}$ kg m^{-2} s^{-1}) occurred through much of the water column during spring ebbs. Most floods also had significant J_s, while neap ebbs showed small J_s. Among the estimated turbulence characteristics, J_s is subject to the most pronounced systematic uncertainty owing to lack of knowledge of the variation of R_f as a function of Ri.

The stress profiles and the turbulent salt flux estimated from the microstructure profiling are compatible with independent estimates based on moored observations of currents, density, and pressure analyzed by Geyer et al. in terms of the integral momentum and salt balances of the estuary. The role of turbulent mixing within the observed flow is qualitatively that envisioned in the early concepts of Pritchard from the 1950s.

1. Introduction

This paper analyzes profiling microstructure observations from the Hudson River estuary taken in August and October 1995. They are part of the larger experiment ''HUDMIX'' designed to quantify the vertical turbulent transports of momentum and salt and to relate them to local and estuary-wide dynamical balances, or, in other words, to analyze how estuarine mixing arises and how it influences the overall estuarine dynamics. The experiment took place in a relatively straight and uniform part of the Hudson River estuary in a deliberate attempt to find a ''simple'' flow and to possibly observe the classical estuarine circulation first proposed by Pritchard (1952, 1954, 1956). In his concept of the mean circulation, freshwater enters from the landward end of the estuary, saltwater enters in the lower layer at the seaward end, and brackish water leaves in the upper layer at the seaward end. The transition from saltwater to brackish water is an irreversible process that can be brought about only by mixing. With this background, it appeared imperative to quantitatively and as directly as possible measure the turbulent mixing, while resolving the relevant tidal and fortnightly variability.

Herein, we discuss how the vertical turbulent salt flux and turbulent stress can be estimated from measured viscous dissipation rates, ε, through intermediary eddy diffusivity and eddy viscosity. On this basis, the depth–time variability of salt flux and stress within tidal and

Corresponding author address: Dr. Hartmut Peters, Rosenstiel School of Marine and Atmospheric Science, University of Miami, 4600 Rickenbacker Causeway, Miami, FL 33149-1098.
E-mail: hpeters@rsmas.miami.edu

fortnightly cycles is analyzed and is shown to be compatible with the integral momentum and salt budgets of the estuary, as observed and analyzed by Geyer et al. (2000). We show that, for conditions of tidally stirred estuaries with sustained low gradient Richardson number, Ri < 0.25, the traditional methods of estimating turbulent fluxes of momentum and mass used in open ocean microstructure work (Busch 1977; Osborn 1980; Gregg 1987) need to incorporate a flux Richardson number (R_f) that varies as a function of Ri. We retain the assumption of steady state in the turbulent kinetic energy (TKE, or k) equation. This assumption is discussed as an aside in an appendix, and it is shown that the observed estuarine turbulence differed in significant ways from turbulent shear flows in laboratory (e.g., Rohr et al. 1988) and direct numerical simulation (e.g., Jacobitz et al. 1997).

This paper expands the analysis of Peters (1997) of an earlier microstructure cruise in the Hudson River and of additional observations from the Hudson River by Peters (1999). A companion paper (Peters and Bokhorst 2000, henceforth referred to as Part I) describes the experiment, observations, instrumentation, environmental conditions, and data reduction, and it analyzes the variability of viscous dissipation rates. Relying on Part I, we do not repeat this information here except for a minimal introduction in section 2. Our method of estimating turbulent mass and momentum fluxes from dissipation data is outlined in section 3, with a discussion of the TKE balance being relegated to an appendix. The depth–time variability of the turbulent salt flux and momentum flux (or stress) are analyzed in sections 4 and 5.

2. Observations

During 12 semidiurnal tidal cycles in August and October 1995, we measured currents with an acoustic Doppler current profiler (ADCP) and stratification, viscous dissipation rates, and turbulent overturning scales with the microstructure profiler Shallow Water Microstructure Profiler (SWAMP). The measurements were taken within the central reach of the salt wedge in a regime of strong tidal currents, mostly strong stratification and large shear in the Hudson River off Manhattan, New York City. Two cruises ''HUDM,'' August 1995, and ''HUDM2,'' October 1995, spanned a weak and a strong neap tide to spring tide transition, respectively. As explained in Part I, the ship was drifting with the tidal currents during the measurements, but we still principally observed temporal variations.

We present the measurements herein as averages in bins of normalized depth z/H and of tidal phase ϕ_{M_2} (see also Part I). The water depth is H, and the height above bottom is z. Averages mostly span two tidal cycles from two consecutive days. The semidiurnal tide consisting of both M_2 and S_2 is represented by slowly varying amplitude $a(t)$ and phase $\phi(t)$, which are found by

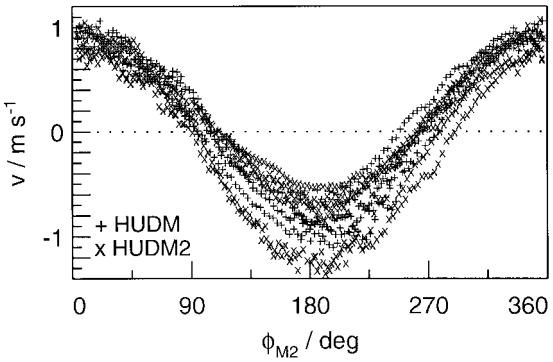

FIG. 1. Depth-averaged along-river currents from cruises HUDM and HUDM2 vs phase of the semidiurnal tide as defined in the text.

complex demodulation of the water level $\zeta(t)$ at The Battery at the southern tip of Manhattan:

$$\zeta(t) = a(t)\cos[\omega_{M2}t + \phi(t)] + n(t) = a(t)\cos[\phi_{M2}(t)] + n(t). \quad (1)$$

Here, variations with frequencies much higher and lower than $\omega_{M_2} = 2\pi/(12.417\text{ h})$ are contained in $n(t)$. Time t assigns values of ϕ_{M_2} to all measurements.

The phase difference between the water level at The Battery and our depth-averaged currents observed with a shipborne ADCP 8–12 km upstream of The Battery was small, such that $0 < \phi_{M_2} < 90°$ and $270° < \phi_{M_2} < 360°$ represent flood, while $90° < \phi_{M_2} < 270°$ is the ebb sector (Fig. 1). Observed depth-averaged currents display fortnightly tidal amplitude variations as well as low-frequency flow variations explained in Part I. We use a coordinate system rotated by 30° such that the y axis parallels the river channel, y increasing landward.

3. Estimating mass flux and stress

a. Dissipation method

In physical oceanography, methods for estimating vertical turbulent fluxes of momentum, mass, and heat from microstructure measurements have commonly been based on the steady-state TKE equation simplified by assuming spatial homogeneity (reviewed by Gregg 1987, 1998). After introducing the concept of eddy coefficients, the homogeneous steady-state TKE equation can be written as

$$P + B = K_m V_z^2 - K_\rho N^2 = \varepsilon \quad (2)$$

with shear production P, buoyancy term B, eddy viscosity K_m, eddy diffusivity K_ρ, square of mean shear $V_z^2 = (\partial\overline{u}/\partial z)^2 + (\partial\overline{v}/\partial z)^2$, and buoyancy frequency N. Here, the mean shear has been written in terms of the horizontal current vector $(\overline{u}, \overline{v})$ and height above bottom, z. The eddy viscosity then follows as

$$K_m = \frac{1}{1 - R_f}\frac{\varepsilon}{V_z^2}. \quad (3)$$

The flux Richardson number is the ratio of buoyancy term and shear production,

$$R_f = -\frac{B}{P} = \frac{K_\rho}{K_m}\frac{N^2}{V_z^2}. \quad (4)$$

With (3), the vertical fluxes of x momentum and y momentum are

$$J_{mx} = -\rho K_m \partial\overline{u}/\partial z \qquad J_{my} = -\rho K_m \partial\overline{v}/\partial z, \quad (5)$$

respectively, and the turbulent stress vector is $\boldsymbol{\tau} = (\tau_x, \tau_y) = -(J_{mx}, J_{my}) = -\mathbf{J}_m$. This procedure is known as ''dissipation method'' (Busch 1977). To our knowledge, it was first applied to oceanic microstructure data by Gregg et al. (1985).

Besides requiring the turbulence to be stationary and in production–dissipation equilibrium, the dissipation method can be valid only when the ''mean'' shear V_z^2 controls the turbulent mixing, a condition expected at small mean gradient Richardson numbers, Ri $\lesssim$ ¼. At large Ri > 1, the production of turbulence is expected to be dominated by fluctuating internal wave-induced shear. Such fluctuating shear is usually filtered out when the mean shear is determined from observations, and numerical circulation models are usually unable to resolve the fluctuating wave-induced shear. A naive application of (3) produces inflated values of K_m at large Ri whenever the resolved V_z^2 underestimates the mostly fluctuating shear available for production of TKE. A discussion of vertical momentum fluxes in the presence of both turbulence and internal waves is beyond the scope of this paper.

In the highly turbulent and strongly sheared flows of estuaries, such as described in Part I and Peters (1997), time constants of thermistors are too large to resolve the diffusive range of the vertical temperature gradient (cf. Gregg 1987). Thus, we were unable to determine the thermal dissipation rate χ, and we cannot use the Osborn–Cox method (Osborn and Cox 1972) for estimating the eddy diffusivity of heat.

This leaves the Osborn method (Osborn 1980) for estimating the eddy diffusivity of mass,

$$K_\rho = \frac{R_f}{1 - R_f}\frac{\varepsilon}{N^2}. \quad (6)$$

At high Reynolds numbers the eddy diffusivity of all scalars should be the same, and, for example, the vertical turbulent salt flux becomes

$$J_S = -\frac{\rho}{1000} K_\rho \frac{\partial S}{\partial z}, \quad (7)$$

where the factor 10^{-3} converts practical salinity to concentration units.

b. Flux Richardson number

It has been commonplace in oceanic microstructure work to assume a constant R_f attaining its maximum value, $R_f/(1 - R_f) \approx 0.2$, a choice consistent with oceanic data (Oakey 1982) but subject to considerable variation (e.g., Moum 1996). This simplification is not permissible here because, in general, R_f cannot be independent of Ri, and because, unlike the oceanic main thermocline, the Hudson estuary exhibits periods of sustained low Ri < 0.25, and even Ri < 0.1, as shown in Part I. It follows from (2) and (4) that $R_f \to 0$ as Ri $\to$ 0 because, in the TKE equation (2), the buoyancy term B approaches 0 with Ri $\to 0$, or $N^2 \to 0$, but neither shear production P nor ε vanish.

Hence, in order to realistically estimate the turbulent mass and salt flux, we need a turbulence model that relates R_f to observable flow variables. We retain the traditional assumption of steady state in the TKE balance. Because existing laboratory and field measurements provide only limited constraints for R_f, we further specify the flux Richardson number as function of Ri alone, $R_f = R_f(\text{Ri})$. We neglect the effect of the Reynolds number Re and of other nondimensional flow variables (Jacobitz et al. 1997). This simplification is appropriate for the energetic, high-Re flow of tidal estuaries.

In the literature, the turbulent Prandtl number is often specified instead of R_f; $\text{Pr}_t = \text{Ri}/R_f$ with (4). In the functional form of $\text{Pr}_t(\text{Ri})$, we follow Schumann and Gerz (1995):

$$\text{Pr}_t(\text{Ri}) = \text{Pr}_t^0 \exp\left(\frac{-\text{Ri}}{\text{Pr}_t^0 R_f^\infty}\right) + \frac{\text{Ri}}{R_f^\infty}. \quad (8)$$

Constants are $\text{Pr}_t^0 = 0.63$, compatible with laboratory and atmospheric data (e.g., Rohr et al. 1988), and $R_f^\infty = 0.19$, compatible with oceanic values (e.g., Moum 1996): the ''mixing efficiency'' $R_f/(1 - R_f)$ is 0.22 at Ri $= 0.25$. Figure 2 displays our $\text{Pr}_t(\text{Ri})$ as well as $R_f/(1 - R_f)$. The latter matches the Rohr et al. (1988) laboratory data well, our main reason for choosing Schumann and Gerz' functional form of $R_f(\text{Ri})$. Note that the coefficient $c_m = 1/(1 - R_f)$ in the dissipation method, (3), deviates little from 1.

The above outlines our approach to estimating turbulent momentum and mass fluxes as an adaptation of the established methods used in oceanic microstructure work to a flow regime with systematic variations of Ri and occurrences of low Ri < 0.25. The introduction of a variable $R_f(\text{Ri})$ is only a modest modification of previous applications of the dissipation and Osborn methods, but it is significant in many flow regimes in and beyond estuaries, wherever low Ri $<$ ¼ occurs.

Maintaining finite R_f for Ri $\to \infty$ allows estimating K_ρ in regimes of low mean shear and high Ri where internal waves may induce turbulence. In practice, approaches with $R_f \to 0$ (e.g., Ivey and Imberger 1991) apply only in laboratory flows, not in natural flows with ubiquitous internal waves. Our results are insensitive to the assumption of finite R_f at large Ri because there is little mixing at large Ri. Setting $R_f = 0$ for Ri > 1 in

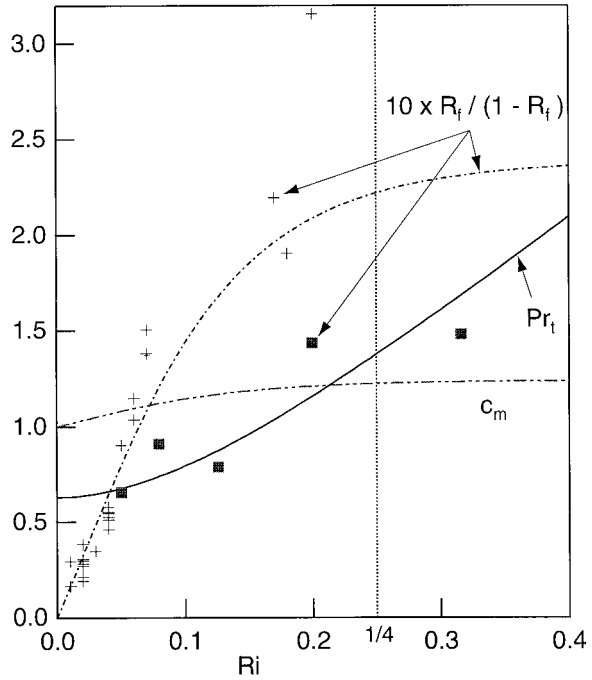

FIG. 2. Turbulence model: turbulent Prandtl number and coefficient of eddy viscosity, $c_m = 1/(1 - R_f)$ [Eq. (3)], and of eddy diffusivity, $R_f/(1 - R_f)$ [Eq. (6)], as a function of Richardson number. Laboratory observations of $R_f/(1 - R_f)$ by Rohr et al. (1988) are given for comparison (plus signs). Solid squares denote estimates of $R_f/(1 - R_f)$ from the Equatorial Undercurrent (Peters et al. 1995).

another sensitivity test reduces the salt flux by typically less than 10%. In principle, it would be desirable to introduce nondimensional flow parameters other than Ri, especially the Reynolds number Re (Jacobitz et al. 1997; Van Atta 1999). It is our impression, however, that the observational basis for constructing a more complete turbulence model with, for example, R_f(Ri, Re, . . .) is insufficient at the present time.

The most important assumptions underlying the approach, steady state, and production–dissipation balance in TKE may need further justification considering the pronounced tidal variations of the turbulence as shown below, in Part I, and in Peters (1997). This topic requires a somewhat involved discussion and yields significant implications, which are, however, not central to the main topic of this paper. Hence, aspects of the TKE balance are analyzed in the appendix. We proceed here to discuss how sensitive the estimated turbulent fluxes are to specifics of our approach, which we refer to as a ''model'' only for the sake of simplicity.

c. Sensitivity to model detail

Equations (3) and (8) imply that the computation of K_m and J_m depends little on $R_f = R_f$(Ri), and thus K_m from variable R_f differs only about 10% from K_m from constant $R_f = 0.167$ [$R_f/(1 - R_f) = 0.2$]. The two traces of K_m in Fig. 3a are not even distinguishable. In contrast, eddy diffusivity and salt flux are sensitive to model

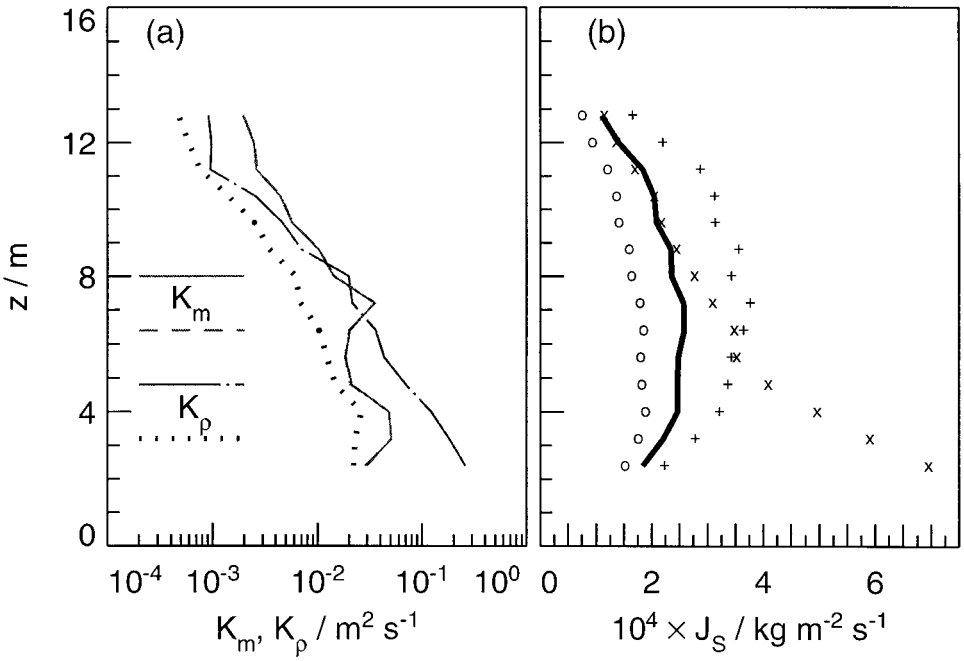

FIG. 3. (a) Average profiles of eddy viscosity [Eq. (3)] and eddy diffusivity [Eq. (6)] of cruise HUDM; results using a variable R_f(Ri) [Eqs. (4), (8)]; solid and dash–dotted lines; results with constant $R_f = 0.167$: dashed and dotted lines. The two traces of K_m are indistinguishable in this log-log plot. (b) Cruise average salt flux from the steady-state model with variable R_f(Ri) and $R_f^\infty = 0.193$ (solid) $R_f^\infty = 0.29$ (+), and $R_f^\infty = 0.13$ (○), and with $R_f = 0.167 = \text{const}$ (×).

assumptions. Constant $R_f = 0.167$ produces cruise average K_ρ up to a factor of 10 larger than the Ri-dependent R_f, and the corresponding J_S increases monotonically toward the bottom (Figs. 3a,c). Such behavior is unrealistic given that boundary conditions dictate $J_S(z = 0) = 0$. Salt flux estimates in Peters (1997) are based on constant $R_f = 0.167$ and are thus significantly overestimated at the smallest Ri.

Here K_ρ and J_S are most sensitive to the parameter R_f^∞ and less to the shape of the function R_f(Ri). When R_f^∞ is increased to 0.29, 50% larger than our standard $R_f^\infty = 0.19$, the cruise average J_S increases proportionately by up to 40% (Fig. 3c). Maximum $J_S(z)$ occur higher in the water column with larger R_f^∞. Figure 2 shows that a value as large as $R_f^\infty = 0.29$ is compatible with laboratory data, and it is compatible with the spread of oceanic data following Moum (1996). Similarly, relatively small values of R_f^∞ cannot be ruled out. In individual turbulent overturns from the Equatorial Undercurrent, Peters et al. (1995a, Fig. 11), for example, found that $R_f/(1 - R_f)$ depended on, and decreased with, decreasing Ri as shown in Fig. 2. The equatorial data are consistent with $R_f^\infty \approx 0.13$. With this value, cruise-averaged J_S are reduced by up to 35% compared to our standard case (Fig. 3b). In general, oceanic turbulence data are not as accurate as laboratory data. However, the ε and χ data of Peters et al. (1995a) were well resolved owing to small profiler fall rates, and were also well calibrated with measured (not nominal) time constant of the thermistor used to detect χ (cf. Gregg 1999).

d. Sensitivity to procedures

The manner in which momentum and mass fluxes are calculated turned out to be even more important than model detail. We compute fluxes from individual microstructure/CTD profiles (drops) combined with 6-min ADCP velocity averages. Averaging the ADCP data is necessary because instrumental noise is prominent in vertical shear, where the velocity noise floor is amplified by a factor of squared vertical wavenumber. The 6-min averaging of ADCP velocity data inevitably produces a sampling mismatch in combination with essentially instantaneous CTD/microstructure data, a problem ameliorated by subsequent ensemble averaging of momentum and mass fluxes and eddy coefficients. Experiments with the data show that the noise in the 6-min shear data does not significantly affect the estimated ensemble-averaged J_S and J_m. These experiments assume a noise variance in shear of 6×10^{-4} s^{-2} based on the manufacturer's specifications, a level roughly consistent with the actual noise floor of the ADCP data.

As an alternative to drop-based estimates, vertical turbulent fluxes can be computed directly from ensemble-averaged velocity/density/dissipation data. Corresponding ensemble-based salt flux estimates are up to factors of 2.5 larger than the respective drop-based flux values. The effect is even stronger in the turbulent momentum flux, ensemble-based estimates often having magnitudes of a decade or more above drop-based values. Drop-based and ensemble-based average momentum fluxes sometimes differ in sign, and ensemble-based momentum flux profiles tend to be very jagged.

Average-based flux estimates are larger than the drop-based estimates because averaging significantly reduces shear variance. Following Peters et al. (1995b), the square of mean shear is

$$\overline{V}_z^2 = \left(\frac{\partial \overline{u}}{\partial z}\right)^2 + \left(\frac{\partial \overline{v}}{\partial z}\right)^2, \tag{9}$$

while the average squared shear is

$$\overline{V_z^2} = \overline{\left(\frac{\partial u}{\partial z}\right)^2} + \overline{\left(\frac{\partial v}{\partial z}\right)^2}, \tag{10}$$

where obviously $\overline{V}_z^2 \leq \overline{V_z^2}$. Ensemble average shear often exhibits $\overline{V}_z^2 \ll \overline{V_z^2}$ (see Fig. 4) simply because shear varies substantially even in tidal flows and even on small spatial and temporal scales. Ensembles of drops taken in consecutive sequences at 1–2 min intervals often contained large variations in shear, stratification, and dissipation rates. It appears that, in inhomogeneous ensembles as ours, $\overline{V}_z^2$ is a poor and ill-conditioned measure of the shear variance available in the generation of turbulence and that $\overline{V_z^2}$ is a better measure as long as it does not contain significant contributions from either turbulence itself or instrumental noise. Computing fluxes from individual drops corresponds more closely to using $\overline{V_z^2}$ than to $\overline{V}_z^2$. Peters et al. (1995a,b) discuss this topic further.

Figure 4 depicts two measures of ''mean'' Richardson numbers corresponding to $\overline{V}_z^2$ and $\overline{V_z^2}$:

$$\overline{\mathrm{Ri}} = \overline{N^2}/\overline{V}_z^2, \qquad \overline{\mathrm{Ri}}_t = \overline{N^2}/\overline{V_z^2}. \tag{11}$$

We note that neither mean shear nor mean Richardson numbers are uniquely defined in stratified flows. These variables are subject to their respective frequency–wavenumber contents.

e. Further considerations

Above, we state that the dissipation method fails at large Ri where the mean flow does not control mixing. Nevertheless, we are still able to obtain valid estimates of the average $\mathbf{J}_m$ because large Ri correspond to small $|\mathbf{J}_m|$, and contribute little to the mean. In observations from the oceanic main thermocline, where mixing is induced by internal gravity waves, estimates of the heat flux from χ via the Osborn–Cox method (Osborn and Cox 1972) and from ε via the Osborn method (6) tend to agree well (Oakey 1982). In analogy, we reason that estimates of J_S are valid even at large Ri.

During flood, currents increasing with height above the bottom have a tendency to advect saltier and heavier water over fresher and lighter water, the tidal straining mechanism of Simpson et al. (1990). The observed mag-

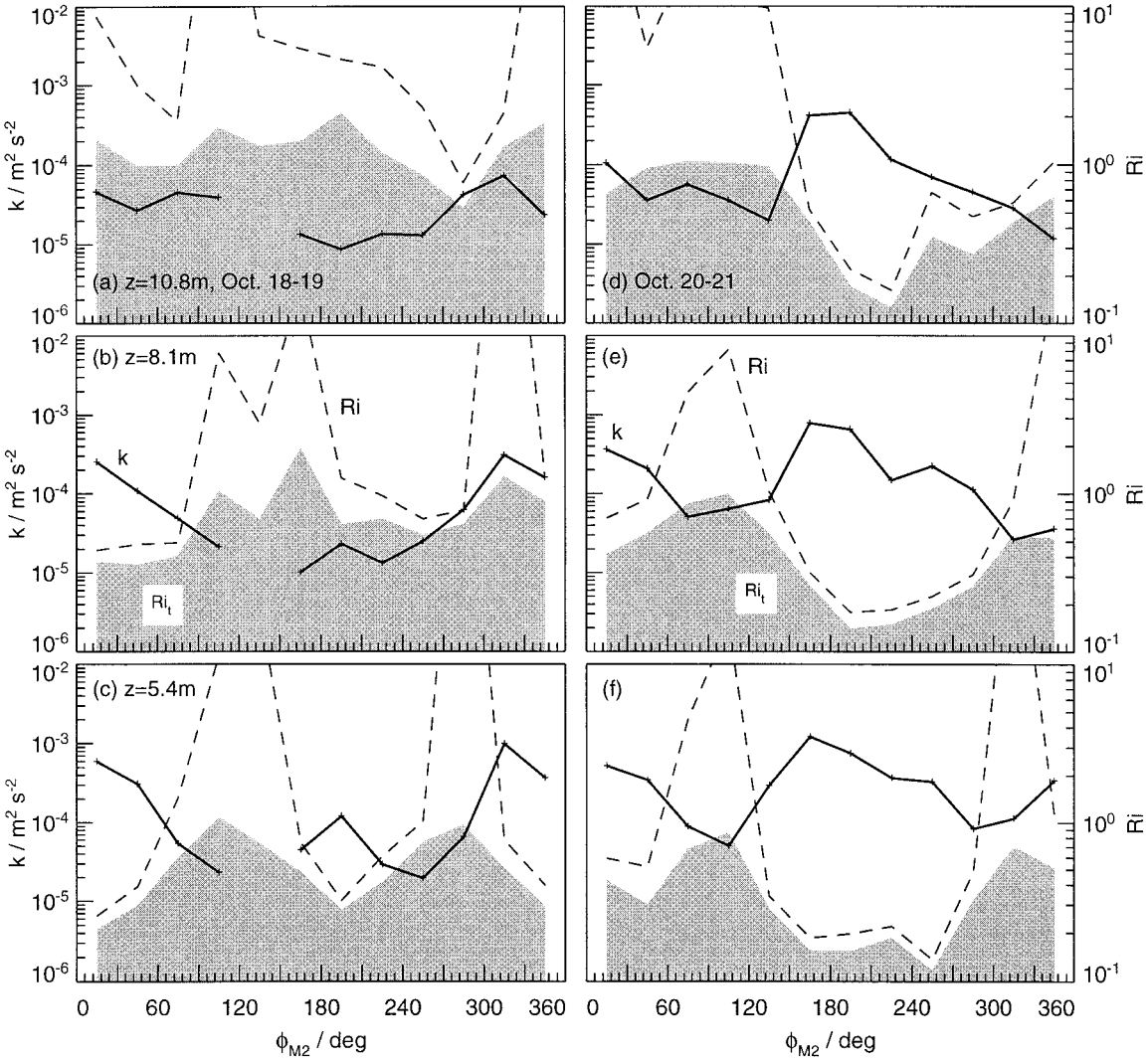

FIG. 4. Turbulent kinetic energy (solid, heavy) and two measures of mean Richardson numbers (shaded and dashed) as function of tidal phase and height above bottom.

nitude of the differential advection is large enough to destabilize the lower water column on a timescale much shorter than tidal. This process affects only the flood tide and only the lowest 2.5–3 m above the bottom—Fig. 5 shows an example profile. Because ADCP velocity profiles do not cover the lowest 3 m we do not estimate turbulent fluxes in this near-bottom zone. It can be shown on the basis of Simpson et al. [1990, Eq. (1)] that even in the statically unstable near-bottom layer shear production dominates over buoyancy production. There is no free convection, and the static instability alters the TKE balance only slightly. Thus, static instability does not pose a problem for our analysis.

The example of an original set of velocity/stratification/microstructure profiles depicted in Fig. 5 serves to provide the reader with a brief impression of our basic observations. (Another example from an ebb tide is shown in Fig. 7 of Part I.) The salinity profile, which also represents density because temperature effects are negligible, shows a very sharp halocline capping an intensely mixing bottom layer with unstable stratification in the lowest 3 m. Above $z = 4.5$ m, N^2 rose fast with increasing height even in the comparatively weakly stratified lower layer. To appreciate typical magnitudes of N^2, we note that $N^2 = 1 \times 10^{-4}$ s^{-2} corresponds to $N = 6$ cph, twice the typical oceanic main thermocline value of 3 cph. It further characterizes the observations that, above $z = 5$ m, Ri rose sharply and $\varepsilon(z)$ fell well below the law-of-the-wall $\varepsilon_b = u_*^3/(\kappa z)$ while it stayed close to ε_b in the lowest 3 m. Here the friction velocity is u_* and von Kármán's constant is κ. Bottom stress $\tau_b = \rho u_*^2$ and u_* were determined from ADCP velocity data as detailed in Part I.

Figure 5d depicts the turbulent displacement ζ_{Th} resulting from Thorpe-sorting salinity from the microconductivity sensor of SWAMP into a monotonic pro-

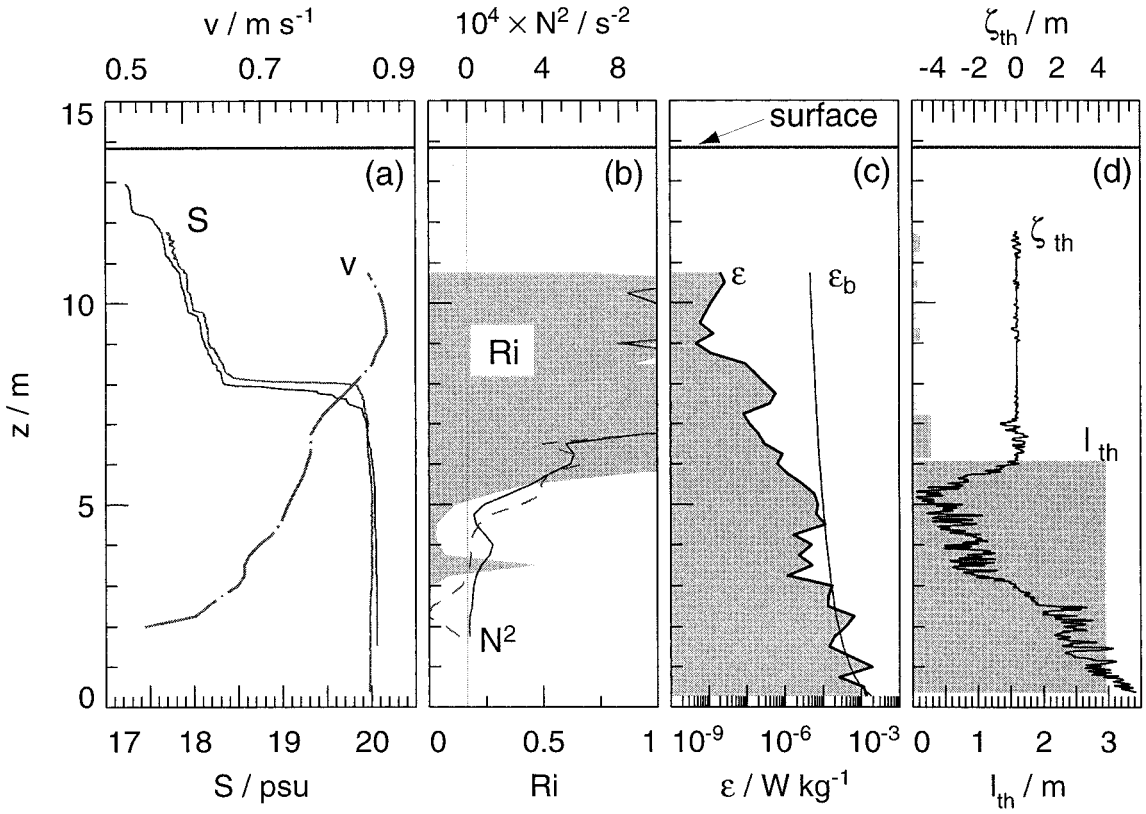

FIG. 5. Example profile of spring flood (drop 6253; 1141 UTC 22 Oct 1995). (a) Along-river velocity and salinity from CTD (Thorpe sorted) and microconductivity cell, the latter showing sharper gradients and instability in the lowest 3 m. (b) Squared buoyancy frequency from sorted (solid) and unsorted (dashed) CTD data; Richardson number based on the sorted CTD–N^2 (shaded). (c) Observed dissipation rate (shaded) and law-of-the-wall dissipation rate ε_b. (d) Displacements and rms displacements resulting from Thorpe-sorting microconductivity.

file. The rms displacement, the Thorpe scale l_{Th}, is also shown. The lowest 3 m were undergoing sustained destabilization due to tidal straining (Simpson et al. 1990), and thus ζ_{th} may not represent actual vertical overturning.

4. Turbulent salt flux and eddy diffusivity

We compute the eddy diffusivity and the vertical turbulent salt flux from individual drops using (6), (7), and (8). Salinity profiles are Thorpe sorted (Thorpe 1977) prior to calculating J_S such that it is always positive. This procedure reduces scatter in drop data but has no significant effect on ensemble averages given that we do not treat the lowest 3 m above the bottom. Even though we compute ensemble averages as a function of normalized depth z/H, we display all data as a function of nominal dimensional depth assuming a mean depth of 16 m.

a. Depth-time variability

Cruise average turbulent salt flux profiles $J_S(z)$ show maxima of about 2×10^{-4} kg m^{-2} s^{-1} at heights of 4–7 m above the bottom in a nominal water depth of $H = 16$ m (Fig. 6). Profiles decrease toward the bottom and the surface. These profiles imply significant average salt transport across the halocline, which had a range of $z = 9$–14 m (Part I and Peters 1997). The vertical structure of $J_S(z)$ differed between the two cruise averages, HUDM showing a broader maximum than HUDM2. Statistical confidence limits of the cruise average profiles indicate a significant difference at $z > 8$ m, but caution is warranted in this assessment because of limitations in sampling. While we were able to measure throughout the evolution from neap tides to spring tides during HUDM2, we were only able to measure during 2 days before neap tides and 3 days at/after spring tides during HUDM (see Part I).

Figure 6 depicts straight arithmetic averages of J_S from drops as well as cruise averages formed from ensemble averages in bins of ϕ_{M2} over 2–3 days duration. The latter allow for a more equal weight of all parts of the tidal period because microstructure drops did not cover tides evenly. The difference between the two sets of cruise averages is insignificant, however. Statistical uncertainty limits were formed by bootstrapping at the 97% confidence level (Efron and Gong 1983). Uncer-

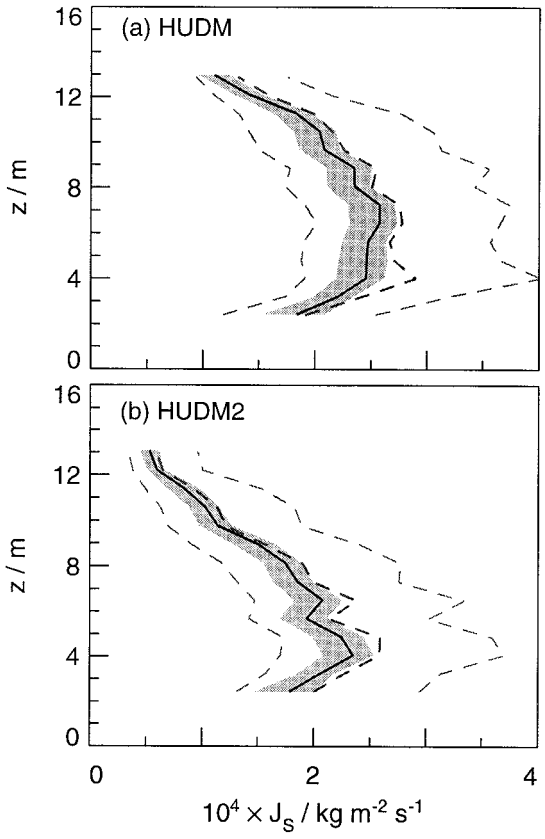

FIG. 6. Cruise average depth profiles of the vertical turbulent salt flux with 97% bootstrap confidence limits: (a) HUDM, (b) HUDM2. Dashed lines: mean from ensemble averages in M_2 phase bins; solid lines with shading: straight mean from drops.

tainty limits of the drop averages are tight, indicating that the random variability of J_S was relatively small and well covered by our data consisting of a total of 2277 drops. These confidence bounds answer the question of how sensitive cruise averages are to the omission of individual drops. In contrast, statistical confidence intervals of the ensemble-based cruise averages are rather wide. They reflect the question how sensitive the mean is to omissions of parts of tidal cycles. Our coverage of tidal cycles was not complete, but gaps were minor. It is likely that the set of narrow confidence limits in Fig. 6 underestimates the true uncertainty, while it may be overly conservative to accept the wider confidence limits.

While cruise average salt flux profiles appear to differ between HUDM and HUDM2, a more detailed analysis of the depth–time variability reveals more similarities in patterns and magnitudes than differences. We discuss HUDM2 because of the better resolution of the neap to spring progression. We depict results as both profiles of J_S (Fig. 7) and time series (Fig. 8). Significant salt flux of 2–8 ($\times 10^{-4}$ kg m^{-2} s^{-1}) occurred during flood over the entire neap–spring cycle, even during neap tide. During neap ebb, in contrast, J_S was very small (Figs. 8a–c).

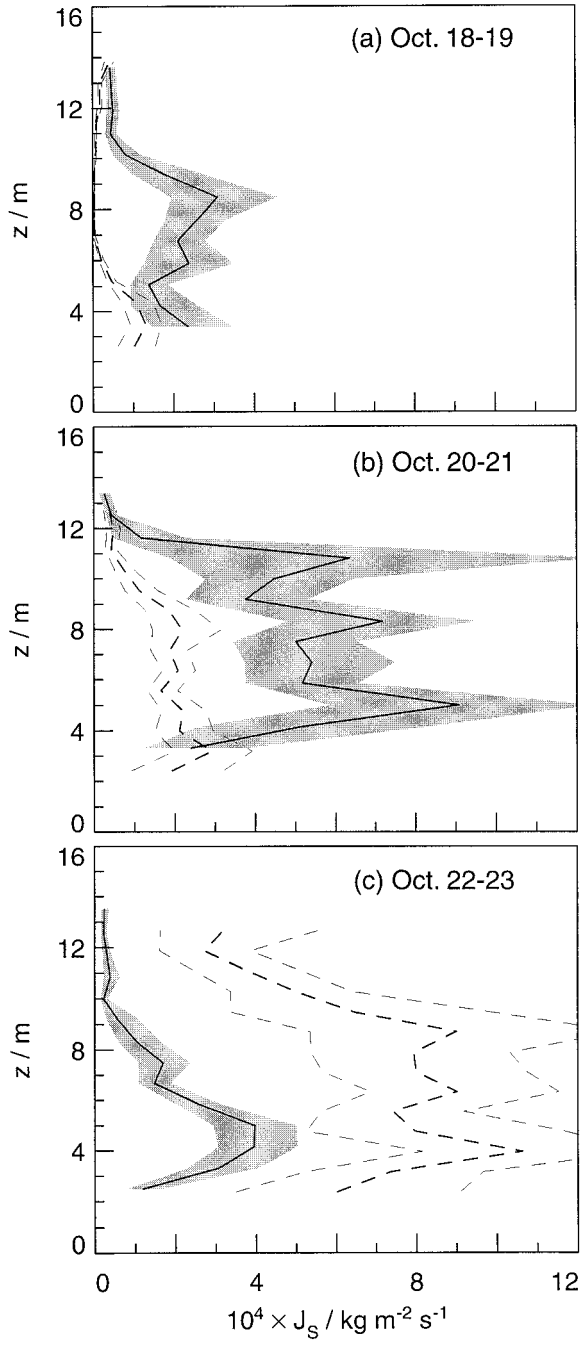

FIG. 7. Turbulent vertical salt flux profiles during flood [Φ_{M2} = 345° [337.5° in (b)]; solid, with confidence limits shaded] and ebb [Φ_{M2} = 165° [202.5° in (b)]; dashed]: (a) neap tide, (b) transition, and (c) spring tide. Flood data in (b) are from 20 Oct only.

During neaps and transition from neaps to springs, salt fluxes were larger during flood than ebb (Figs. 7a–b). Ebb tide J_S grew slowly from 18–19 to 20–21 October and then dramatically to 22–23 October, while flood tide J_S actually decreased from 20–21 to 22–23 October (Figs. 7b–c, 7d–i).

This latter decrease is a result of reduced ε even more

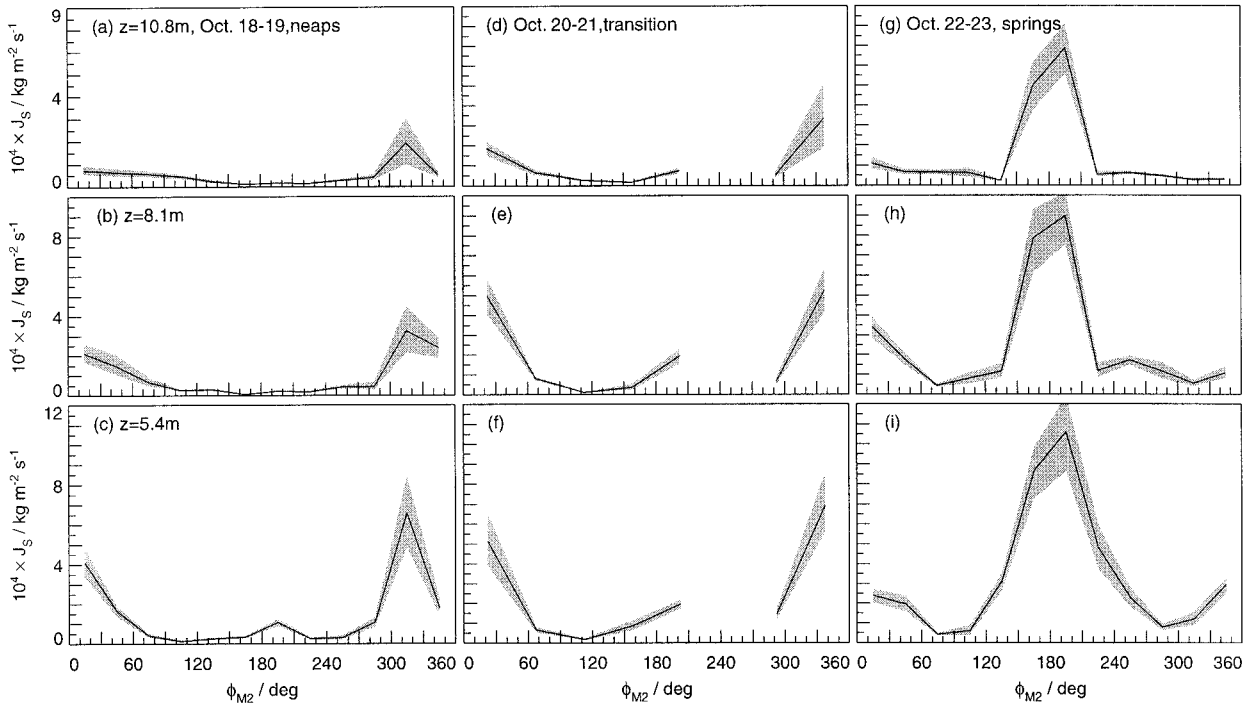

FIG. 8. Vertical turbulent salt flux as a function of semidiurnal tidal phase, cruise HUDM2. (a)–(c) Average of 18–19 Oct 1995 (neap tide), (d)–(f) 20–21 Oct, (g)–(i) 22–23 Oct (spring tide). Data are from heights above the bottom of (a), (d), (g): 10.8 ± 1.4 m; (b), (e), (h): 8.1 ± 1.4 m; (c), (f), (i): 5.4 ± 1.4 m. Shading indicates statistical confidence limits.

than reduced stratification. Variations in mixing between 20–21 and 22–23 October are only partly attributable to increased tidal amplitude within the fortnightly cycle. Complications arise from remotely forced low-frequency currents in the Hudson with excess inflow and boosted floods on 20–21 October and excess outflow and boosted ebbs on 22–23 October (cf. Part I).

The largest J_S overall, and especially high up in the water column, appeared during spring ebb with 2-day average values of 7–11 ($\times 10^{-4}$ kg m^{-2} s^{-1}) (Figs. 8 and 7). These large values are associated with the intense turbulent mixing spanning the water column during spring ebb (cf. Part I; Peters 1997). Figure 7 further shows large J_S during transition flood and smaller, but still significant, salt flux even during neap flood. Except during spring ebb, J_S was small—but not negligible—at $z \gtrsim 12$ m, indicating weak mixing across the halocline (cf. Peters 1997). Mixing in the halocline is important because it provides the turbulent exchange between the lower salty and upper brackish layer.

Figure 8 displays J_S at a rather coarse resolution in tidal phase and time, equivalent to 1 h, and thus phase differences in the vertical are not well discernible. During cruise HUDM2 shown in Fig. 8, the vertical phase delay of mixing variables was smaller than during cruise HUD1 analyzed by Peters (1997). A progressive delay of mixing with increasing height above the bottom was also observed in the Irish Sea by Simpson et al. (1996).

b. Eddy diffusivity

The eddy diffusivity is an important turbulence characteristic in its own right, not merely a step on the way toward estimating the mass flux. Figure 9 depicts $K_\rho(z)$ for fully developed floods and ebbs during neap, transition, and spring conditions. Minima of 10^{-5} m^2 s^{-1} occurred high in the water column in the halocline, while maxima of about 2–5 ($\times 10^{-2}$ m^2 s^{-1}) occurred in the lowest 4 m. Note that K_ρ varied by 2–3 decades throughout the water column. Increases in K_ρ from neap to spring tides were most pronounced in the upper water column. The depth–time variations of J_S depicted in Fig. 7 largely reflect the corresponding variations of K_ρ depicted in Fig. 9 even though the vertical salinity gradient also plays a role. The influence of K_ρ tends to dominate over $\partial S/\partial z$ because of the large logarithmic variability of ε.

Because the Hudson River estuary remains stratified throughout the fortnightly cycle, currents are baroclinic and shear does not entirely vanish even around slack tides (Part I). Consequently, mixing was comparatively weak but not absent at slack tides. The smallest observed ensemble-averaged K_ρ were about 6×10^{-6} m^2 s^{-1} at $z \approx 8$ m and about 10^{-4} m^2 s^{-1} near $z = 3$ m (not shown).

c. Diffusive timescale

Peters (1997) has already pointed out that turbulent salt fluxes as large as those observed during spring ebb

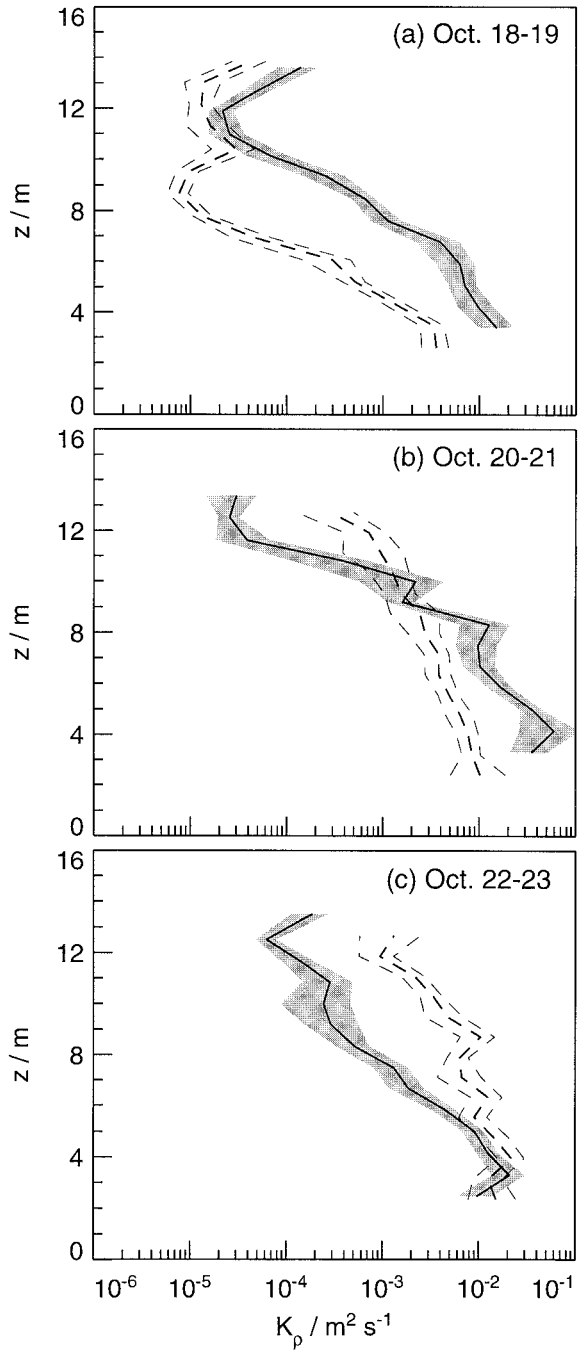

FIG. 9. Eddy diffusivity during flood (solid, with confidence limits shaded) and ebb (dashed): (a) neap tide, (b) transition, and (c) spring tide. Ebb and flood are defined as in Fig. 7.

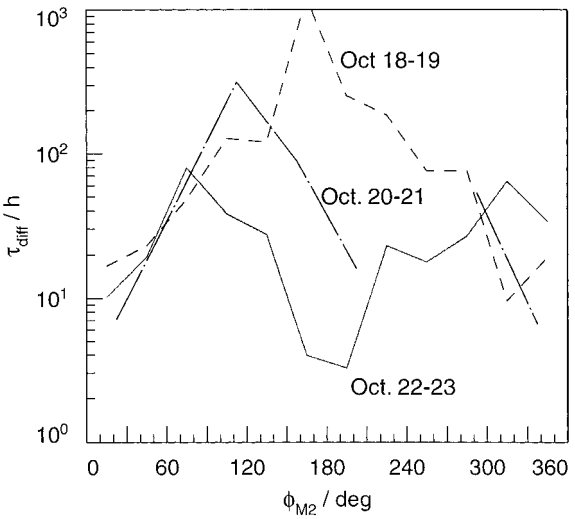

FIG. 10. Diffusive timescale of the vertical turbulent salt flux working toward eliminating the haline stratification, cruise HUDM2. Note that τ_{diff} became smaller than the M_2 period during spring ebb.

work to eliminate the stratification on a timescale smaller than that of the semidiurnal tide. We estimate a diffusive timescale τ_{diff} as the ratio of the salt anomaly in the upper half of the water column, $10^{-3}\int_{H/2}^{H}\rho[S(z) - S(H/2)]\,dz$, to the salt flux $J_S(z = H/2)$ shown in Figs. 8b,e,f. Figure 10 depicts τ_{diff} as a function of M_2 phase and neap-spring progression. Diffusive timescales were much larger than the M_2 period during neap ebb, of the order of the M_2 period during all floods, and as small as 4 h during spring ebb.

Small τ_{diff} occurred throughout the fortnightly cycle, an indication that turbulent mixing was affecting the stratification not just during spring tide. When the middepth salt flux shown in Fig. 8 is integrated over a fortnight, it is found that spring ebb contributes about 30% of the total, and transition ebb and neap ebb contribute another 8% and 1.5%, respectively. The remainder of the total salt flux is provided by flood tides at a fairly even rate over the fortnight.

d. Comparison of J_S with the integral salt balance

Geyer et al. (2000) analyze the integral momentum balance of the same stretch of the Hudson estuary treated herein based on moored velocity, density, and pressure measurements taken over 2½ months time span with HUDM at the beginning and HUDM2 at the end. R. Geyer (1999, personal communication) has also analyzed the integral salt balance, but examining the integral salt balance is more difficult than analyzing the integral momentum balance owing to the dominance of lateral advection. The salt balance equation,

$$\frac{\partial S}{\partial t} + u\frac{\partial S}{\partial x} + v\frac{\partial S}{\partial y} + w\frac{\partial S}{\partial z} - \frac{\partial}{\partial z}\left(K_\rho\frac{\partial S}{\partial z}\right) - K_H\left(\frac{\partial^2 S}{\partial x^2} + \frac{\partial^2 S}{\partial y^2}\right) = 0, \quad (12)$$

can be rewritten in terms of vertical and horizontal advective and diffusive fluxes as

$$\frac{\partial S}{\partial t} + \frac{\partial J_{Su}}{\partial x} + \frac{\partial J_{Sv}}{\partial y} + \frac{\partial J_{Sw}}{\partial z} + \frac{\partial J_S}{\partial z} + \nabla_H \cdot \mathbf{J}_{SH} = 0, \quad (13)$$

where the correspondence of terms between (12) and

(13) defines the various flux components in an obvious manner.

Spanwise advection (J_{Sv}) and horizontal mixing ($\mathbf{J}_{SH}$) were probably small, but vertical advection (J_{Sw}) cannot be neglected at least during flood owing to vertical velocities induced by the upstream influence of hydraulic processes associated with bathymetric variability near the George Washington Bridge, about 7 km north of our locale (Chant 1995; Chant and Wilson 1997). The upward movement of the halocline during neap flood is clearly seen in Fig. 5b of Part I. The moored observations of Geyer et al. (2000) determine $\partial S/\partial t$ and streamwise advection (J_{Sv}), while the sum of all other terms appears as residual. The vertical velocity could not be determined with sufficient accuracy to separate the diffusive (J_S) and advective component (J_{Sw}) of the total vertical salt flux.

Neglecting small terms, averaging in the vertical from the bottom ($z = 0$) to height h, and replacing differentiation in y with finite differences ($\Delta y = 7$ km) yields the integral salt balance examined by R. Geyer (1999, personal communication),

$$\int_0^h \frac{\Delta J_{Sv}}{\Delta y}\, dz + J_{SR}(h) = 0, \qquad (14)$$

where J_{SR} is the residual vertical salt flux. Its 2½-month average at middepth is $J_{SR} = 1.5 \times 10^{-4}$ kg m^{-2} s^{-1}. Larger tidally averaged fluxes of up to 4×10^{-4} kg m^{-2} s^{-1} occurred during neap tides. The above average J_{SR} compares favorably with our turbulent salt flux estimates. Averaging over fortnightly cycles, we find diffusive salt transports at middepth of $J_S = 1.7 \times 10^{-4}$ kg m^{-2} s^{-1} for HUDM2 and 2.4×10^{-4} kg m^{-2} s^{-1} for HUDM.

Considering that vertical advection must have carried some fraction of J_{SR} and that J_{Sw} and J_S are both positive, the comparison of J_{SR} and J_S suggests that we might be overestimating the turbulent salt flux. Pragmatically we chose $R_f^\infty = 0.19$ following previous microstructure work while considering laboratory and oceanic data. Choosing a smaller R_f^∞ compatible with the uncertainty limits indicated in section 3 above might produce a better match of J_{SR} and J_S. This conclusion has to remain tentative, however, because of the mismatch in sampling between microstructure data and integral salt balance, and because terms of the salt budget remain undetermined. Despite this uncertainty, we can conclude that turbulent mixing carried a substantial part of the vertical salt transport needed within Pritchard's concept of estuarine salt balance briefly introduced in section 1.

5. Turbulent stress and eddy viscosity

Eddy viscosity, momentum flux, and stress are computed from microstructure drop data and 6-min ADCP velocity data using (3), (5), and (8). These estimates of internal turbulent stress are compared with the bottom shear stress τ_{by}, determined independently from the ADCP velocity at $z \approx 2.5$ m using a quadratic drag law with drag coefficient $c_d = 0.002$. Trowbridge et al. (1999) directly measured the Reynolds stress and found departures from logarithmic velocity profiles in the lowest 2–3 m above the bottom. Similarly, Part I shows deviations from law-of-the-wall scaling. Due to these complications, the exact drag coefficient for $z = 2.5$ m is not known, a range of 0.002–0.0025 being compatible with the direct stress measurements.

a. Depth-time variability

The largest internal along-river turbulent stress τ_y occurred during spring ebbs and transition floods with values of -0.8 Pa and 1 Pa at $z = 5.4$ m, respectively (Figs. 11i,f). The corresponding bottom stress values were -1.1 Pa and 0.95 Pa. High in the water column at $z = 10.8$ m, the stress was substantially with -0.4 Pa during spring ebbs and much smaller in magnitude otherwise (Fig. 11g). Neap ebbs had small stress magnitudes absolute and relative to the bottom stress, a finding that even holds low in the water column at $z = 5.4$ m where neap floods show significant internal stress (Figs. 11a–c). Flood tide τ_y decreased from transition to springs at all depths in apparent response to low-frequency flow boosting floods during transition and reducing them during springs (cf. section 4 above and Part I). Spring floods had especially small τ_y in the upper water column (Fig. 11g).

As argued in Part I, the intense mixing during spring ebb resulted from shear instability in strong stratification. Part I furthermore shows large Ri near the bottom during neap ebb, and thus the small $|\tau_y|$ at $z \geq 5.4$ m of neap ebbs is attributable to stable stratification and suppression of shear instability.

Profiles of turbulent stress depicted in Fig. 12 were approximately linear between bottom and surface during spring ebbs and concave otherwise, showing very small $|\tau_y|$ in the upper 4–6 m. Dotted lines provide a visual aid for extrapolating the internal stress τ_y to the bottom stress τ_{by}. In this, the constant stress layer of thickness 1–2 m has been ignored. Seemingly anomalous negative τ_y occurred high in the water column during flood, when τ_y is mostly positive. The feature is more easily visible in Fig. 11a than in Fig. 12. The $\tau_y < 0$ results from the decrease of $v(z)$ toward the surface from its maximum in the flood jet (Part I). We assume that the turbulent diffusion of momentum follows a flux-gradient law, and thus the estimated along-river stress has the opposite sign above the flood jet than below it.

b. Eddy viscosity

Depth–time variations of the eddy viscosity during fully developed ebbs and floods shown in Fig. 13 are similar to those of K_ρ discussed above, except that K_m varied only by 1–2 decades over the water column, while K_ρ ranged over 2–3 decades. The difference be-

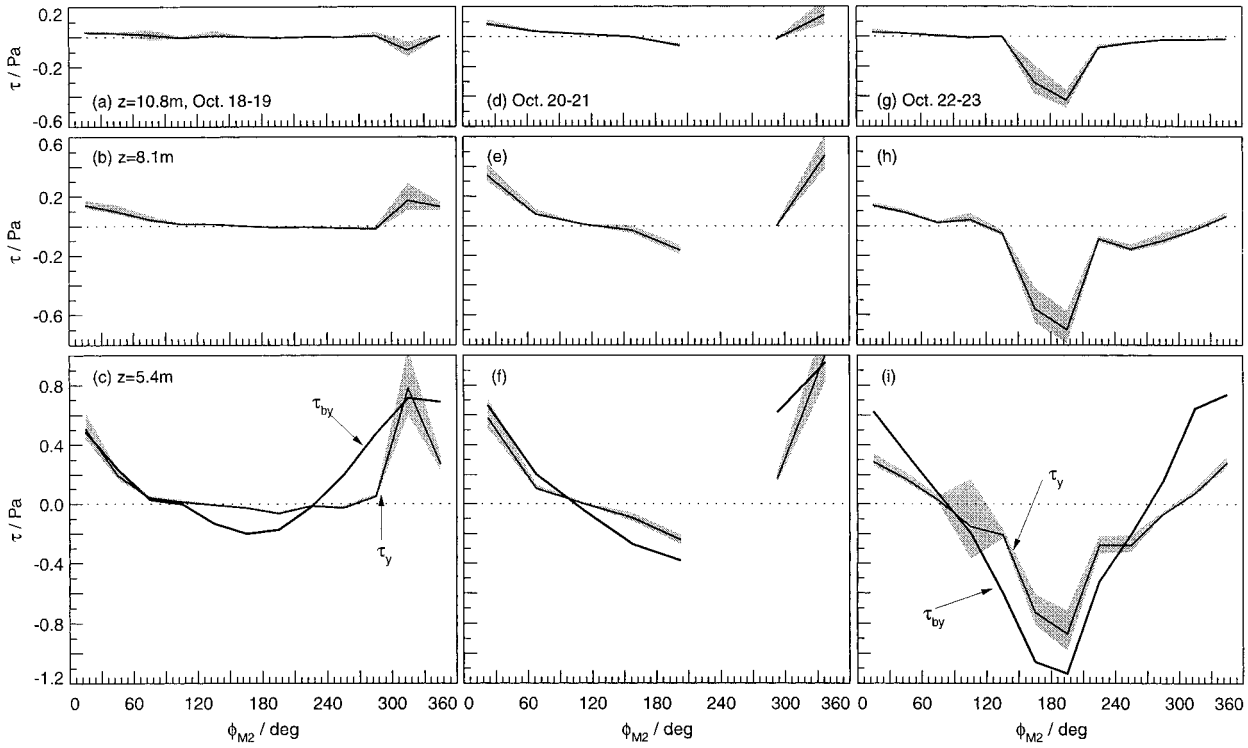

FIG. 11. Along-river bottom stress and internal stress as a function of semidiurnal tidal phase, cruise HUDM2, (a)–(c) Average of 18–19 Oct 1995, (d)–(f) 20–21 Oct, (g)–(i) 22–23 Oct. Data are from heights above the bottom of (a), (d), (g): 10.8 ± 1.4 m; (b), (e), (h): 8.1 ± 1.4 m; (c), (f), (i): 5.4 ± 1.4 m. Shading indicates statistical confidence limits.

tween K_m and K_ρ is given by $\mathrm{Pr}_t(\mathrm{Ri})$ as specified in (8). A general increase of Ri with increasing height above bottom (Part I) corresponds to an increase in Pr_t. Fortnightly variations of K_m were largest in the upper water column, and some of the largest K_m occurred during the transition from neaps to springs. The smallest K_m observed near slack tide were about 6×10^{-5} m^2 s^{-1} at $z > 8$ m and 8×10^{-4} m^2 s^{-1} at $z \approx 3$ m, respectively (not shown).

c. Comparison with the integral momentum balance

Geyer et al. (2000) discuss the momentum balance of the estuarine flow on the basis of the equation

$$\tau_e(h) = -\int_0^h \left(\rho \frac{\partial v}{\partial t} + \frac{\partial p}{\partial x}\right) dz + \tau_s, \qquad (15)$$

which has been adapted to our conventions. Here $\partial p/\partial x$ is the sum of barotropic and baroclinic pressure gradient, τ_s is the surface stress, and τ_e is an ''effective stress,'' which lumps together advective contributions and vertical mixing of momentum. The 2½-month average of this residual of the momentum balance is shown in Fig. 14 for maximum ebb tide and flood tide, and for neap and spring conditions. Our corresponding estimates of the vertical turbulent stress from HUDM and HUDM2 are also depicted, each curve representing an average of two semidiurnal cycles from two consecutive days. There is a similar sampling mismatch as in the case of the salt flux discussed above.

Nevertheless, Fig. 14 shows that the two kinds of stress estimates coincide very closely during spring ebbs and also match fairly well during HUDM neap flood. All neap ebbs as well as the HUDM2 spring flood show turbulent stress of about one-third of the residual of the momentum balance, while the turbulent estimate exceeds the momentum balance residual during HUDM2 neap flood. This latter anomaly appears to be related to the substantial inflow into the estuary at the time (Part I) resulting in rather large bottom stress and stress in the water column. We conclude that, even though the comparison of the tidal momentum balance of Geyer et al. (2000) with our turbulent stress estimates is limited by sampling mismatch, the two independent estimates are compatible with each other. As in the case of the salt balance, we find that our observations qualitatively fit the Pritchard concept of estuarine dynamics introduced in section 1.

6. Conclusions

Part of the scientific effort presented herein was spent on developing a method of realistically estimating eddy viscosity, eddy diffusivity, and turbulent fluxes of momentum and salt from observed ε, currents, and strat-

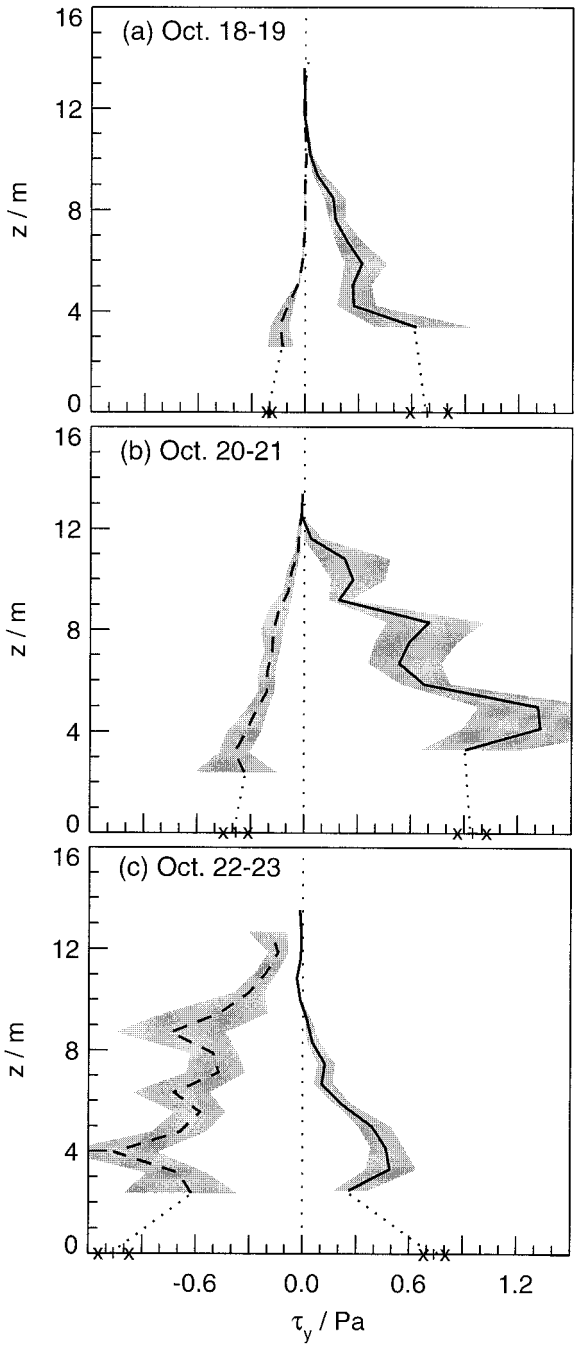

FIG. 12. Along-river turbulent stress at the bottom and in the water column from HUDM2: (a) neap tide, (b) transition, and (c) spring tide. Ebb (dashed) and flood (solid) are defined as in Fig. 7. Bootstrap uncertainty limits are indicated throughout.

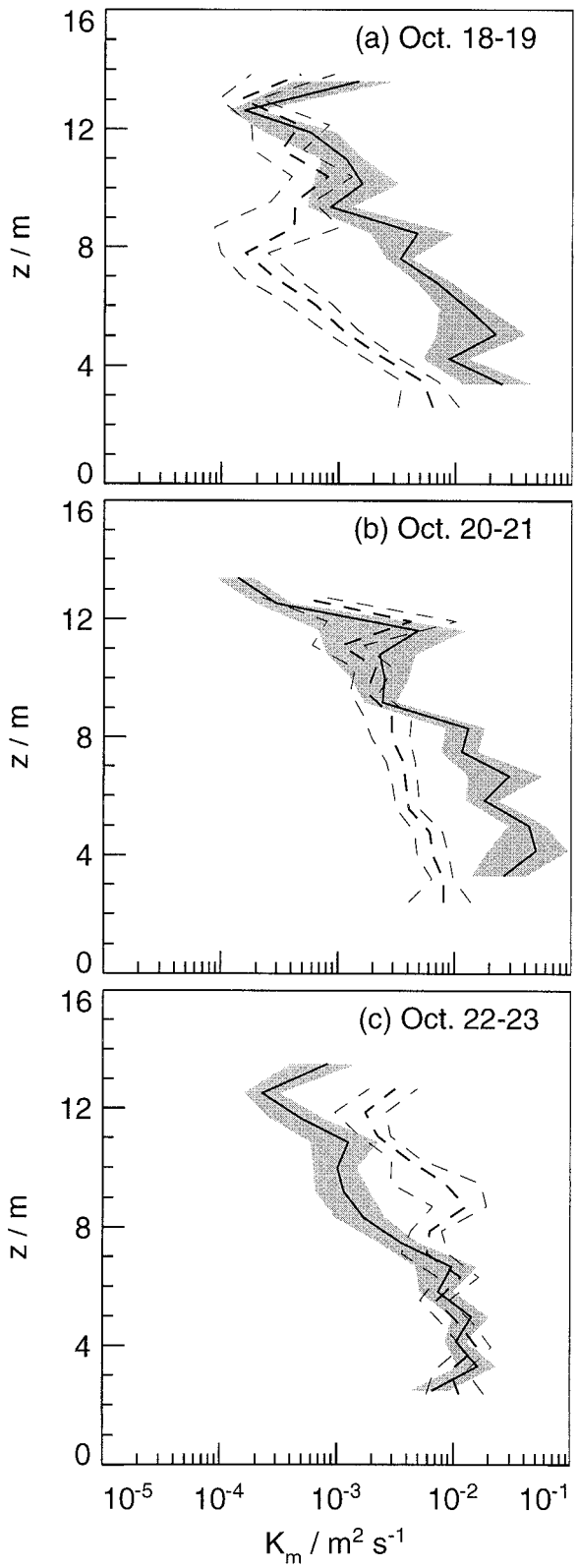

FIG. 13. Eddy viscosity during flood (solid, with bootstrap confidence limits shaded) and ebb (dashed): (a) neap tide, (b) transition, and (c) spring tide. Ebb and flood are defined as in Fig. 7.

ification. Sustained low gradient Richardson numbers occurring in the Hudson and similar estuaries have to be accounted for. At a minimum, the flux Richardson number needs to be modeled as a function of the gradient Richardson number in the traditional dissipation method (Busch 1977) and Osborn method (Osborn, 1980). As argued in the appendix, we had to retain the

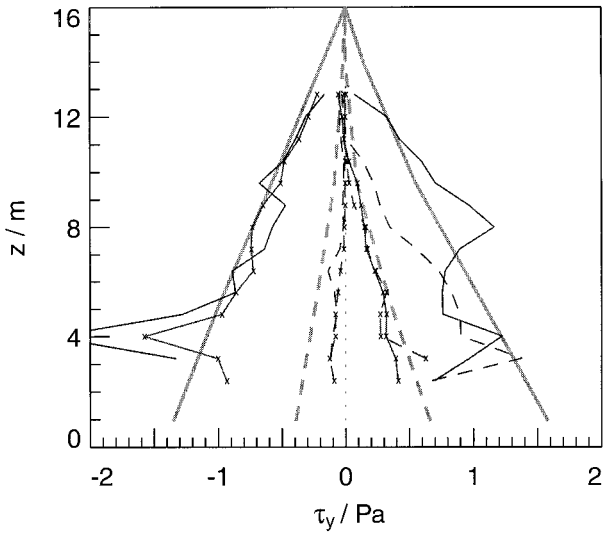

FIG. 14. Maximum streamwise stress during ebb and flood and neaps (dashed) and springs (solid) from the integral momentum balance of Geyer et al. (2000) (thick lines), HUDM (thin lines), and HUDM2 (thin lines with *x* symbols).

assumption of steady state in the turbulent kinetic energy budget and reject recent nonstationary analytical turbulence models (Van Atta 1999; Baumert and Peters 2000).

According to our experience, the dynamics of stratified estuarine turbulence are sufficiently complex that, in the sense of predictive models, they appear to be commensurate only with numerical modeling, while simplified analytical approaches fail. At a diagnostic level, however, the prevalence of steady state in the TKE balance enables realistic estimates of turbulent momentum and mass fluxes from observed dissipation rates. Currently, the accuracy of these estimates is limited by insufficient knowledge of how the flux Richardson varies as a function of gradient Richardson number, Reynolds number, and other flow parameters. Nevertheless we show that the estimated diapycnal eddy diffusivity, eddy viscosity, turbulent salt flux, and stress are compatible with independent estimates based on moored observations and tidal dynamics. In the stretch of the Hudson investigated, vertical mixing indeed plays the role envisioned much earlier by Pritchard (1952, 1954, 1956).

We discuss how mixing characteristically varies as a function of depth, tidal phase, and fortnightly cycle. A summary is provided in the abstract and therefore not repeated here. These variations of mixing are loosely related to variations in gradient Richardson numbers as described by Peters (1997) and in Part I. We have refrained from restating this topic because quantitative predictions of mixing require numerical modeling as argued above. In this context, our measurements can become useful beyond their geographic origin by serving as an observational basis for testing and improving turbulence closure models, work currently under way and to be published separately. At a purely observational level, we expect our findings to be characteristic of turbulent mixing not only in the Hudson River but also in other partially mixed tidal estuaries.

Acknowledgments. The experiment ''Stress, Salt Flux and Dynamics of a Partially Mixed Estuary'' was funded by the National Science Foundation (OCE 9415582/9796016). The turbulence modeling presented herein evolved from collaboration with Helmut Baumert, to whom we are greatly indebted. In addition to the many people whose substantial contributions are acknowledged in Part I, we would like to thank John Trowbridge, John Simpson, and an anonymous reviewer for sharing their scientific insight, and Jossy Jacob for sustained assistance.

APPENDIX

TKE Balance

In section 3 above, we postponed discussing the assumptions of steady state and production–dissipation balance in the TKE. These assumptions are supported by ongoing work of numerically simulating mixing in the Hudson estuary. In collaboration with H. Baumert, we are employing a k–ε turbulence closure model adapted from Burchard and Baumert (1995) and Regener et al. (1997). The simulations reproduce both the observed $\varepsilon(z, t)$ and $l_{\mathrm{Th}}(z, t)$ well. The model stays in production–dissipation balance most of the time except for short transients associated with the onset of ebb and flood, a feature robust with respect to variations of model constants. The nonstationary TKE equation can be written as

$$\frac{dk}{dt} + \mathrm{diff}(k) = P + B - \varepsilon \qquad \text{(A1)}$$

in analogy to (2). The ''turbulence diffusion'' diff(k) parameterizes the pressure work and triple correlation terms in a form representing the self-induced spreading of TKE. Mostly, our numerical model runs maintain $|dk/dt| \ll P$ and $|\mathrm{diff}(k)| \ll P$ such that the assumption of steady state in TKE, (2), is justified.

A further question is whether estimates of turbulent momentum and mass fluxes could be improved by employing nonstationary turbulence models such as those of Van Atta (1999) or Baumert and Peters (2000). These analytical models are constructed such as to reproduce the most basic behavior of turbulence in unbounded homogeneous stratified shear flow: exponential growth of TKE at sufficiently low Ri, steady state of TKE at some Richardson number Ri_s, and exponential decay at $\mathrm{Ri} > \mathrm{Ri}_s$. This behavior is found, for example, in the laboratory experiments of Rohr et al. (1988) and the numerical model runs of Jacobitz et al. (1997). Within the nonstationary models named above, deviations from steady state in TKE are large at sufficiently low Ri. In

Baumert and Peters (2000) as well as, for example, in Mellor and Yamada (1982), $K_m = 2\varepsilon V_z^2$ holds in the limit $\mathrm{Ri} \to 0$, while a production–dissipation balance implies $K_m = \varepsilon V_z^2$ as stated in (3).

The analytical turbulence models of Van Atta (1999) and Baumert and Peters (2000) thus predict growth of k at sufficiently small Ri and the fastest growth at the smallest Ri. Our turbulence observations do not follow this pattern in any way as shown in Fig. 4. The observed k is roughly inversely correlated with Ri, and k tends to *decrease* during phases of low mean Ri, especially during spring ebb (Figs. 4g–i, $120° < \Phi_{M2} < 180°$). During this latter period, Ri was clearly smaller than any plausible Ri_s. Further, k is seen to *increase* during periods of large Ri exceeding any plausible Ri_s. The preceding discussion can be based on either measure of mean Richardson number defined in (11), $\overline{\mathrm{Ri}}$, or $\overline{\mathrm{Ri}_t}$. In constructing Fig. 4, we estimate the TKE from the measured ε and measured Thorpe (1977) scales, l_{Th}, via Taylor scaling (Taylor 1935), $\varepsilon = c_k k^{3/2} l_{\mathrm{Th}}^{-1}$. Because the value of c_k does not matter for our discussion, we let $c_k = 1$.

Diagnosing the problem on the basis of our numerical k–ε modeling, we find that the turbulence diffusion $\mathrm{diff}(k)$ typically is as large as the tendency dk/dt and greatly affects the nonstationary evolution of k. Owing to the requirement of homogeneity, turbulence diffusion does not appear in the analytical models. We conclude that estuarine flow such as in the Hudson differs fundamentally from unbounded homogeneous shear flows and that the models of Van Atta (1999) and Baumert and Peters (2000) are not applicable.

REFERENCES

Baumert, H., and H. Peters, 2000: Second moment closures and length scales for stratified turbulent shear flows. *J. Geophys. Res.,* **105,** 6453–6468.

Burchard, H., and H. Baumert, 1995: On the performance of a mixed-layer model based on the k–ϵ turbulence closure. *J. Geophys. Res.,* **100,** 8523–8540.

Busch, N. E., 1977: Fluxes in the surface boundary layer over the sea. *Modelling and Prediction of the Upper Layers of the Ocean,* E. B. Kraus, Ed., Pergamon, 72–91.

Chant, R., 1995: Tidal dynamics of the Hudson River estuary. Ph.D. thesis, Marine Sciences Research Center, SUNY at Stony Brook. [Available from Marine Sciences Research Center, SUNY at Stony Brook, Stony Brook, NY 11794-5000.]

——, and R. E. Wilson, 1997: Secondary circulation in a highly stratified estuary. *J. Geophys. Res.,* **102,** 23 207–23 215.

Efron, B., and G. Gong, 1983: A leisurely look at the bootstrap, the jackknife, and cross-validation. *Amer. Stat.,* **37,** 36–48.

Geyer, W. R., J. H. Trowbridge, and M. M. Bowen, 2000: The dynamics of a partially mixed estuary. *J. Phys. Oceanogr.,* **30,** 2035–2048.

Gregg, M. C., 1987: Diapycnal mixing in the thermocline: A review. *J. Geophys. Res.,* **92,** 5249–5286.

——, 1998: Estimation and geography of diapycnal mixing in the stratified ocean. *Physical Processes in Lakes and Oceans.* Vol. 54, *Coastal and Estuarine Studies,* J. Imberger, Ed., Amer. Geophys. Union, 305–338.

——, 1999: Uncertainties and limitations in measuring ϵ and χ_t. *J. Atmos. Oceanic Technol.,* **16,** 1483–1490.

——, H. Peters, J. C. Wesson, N. S. Oakey, and T. J. Shay, 1985: Intensive measurements of turbulence and shear in the equatorial undercurrent. *Nature,* **318,** 140–144.

Ivey, G. N., and J. Imberger, 1991: On the nature of turbulence in a stratified fluid. Part I: The energetics of mixing. *J. Phys. Oceanogr.,* **21,** 650–658.

Jacobitz, F., S. Sarkar, and C. W. Van Atta, 1997: Direct numerical simulations of the turbulence evolution in a uniformly sheared and stably stratified flow. *J. Fluid Mech.,* **342,** 231–261.

Mellor, G. L., and T. Yamada, 1982: Development of a turbulence closure model for geophysical fluid problems. *Rev. Geophys. Space Phys.,* **20,** 851–875.

Moum, J. N., 1996: Efficiency of mixing in the main thermocline. *J. Geophys. Res.,* **101,** 12 057–12 070.

Oakey, N. S., 1982: Determination of the rate of dissipation of turbulent energy from simultaneous temperature and velocity shear microstructure measurements. *J. Phys. Oceanogr.,* **12,** 256–271.

Osborn, T. R., 1980: Estimates of the local rate of vertical diffusion from dissipation measurements. *J. Phys. Oceanogr.,* **10,** 83–89.

——, and C. S. Cox, 1972: Oceanic fine structure. *Geophys. Fluid Dyn.,* **3,** 321–345.

Peters, H., 1997: Observations of stratified turbulent mixing in an estuary. Neap-to-spring variations during high river flow. *Estuarine Coastal Shelf Sci.,* **45,** 69–88.

——, 1999: Spatial and temporal variability of turbulent mixing in an estuary. *J. Mar. Res.,* **57,** 805–845.

——, and R. Bokhorst, 2000: Microstructure observations of turbulent mixing in a partially mixed estuary. Part I: Dissipation rate. *J. Phys. Oceanogr.,* **30,** 1232–l244.

——, M. C. Gregg, and T. B. Sanford, 1995a: Detail and scaling of turbulent overturns in the Pacific Equatorial Undercurrent. *J. Geophys. Res.,* **100,** 18 349–18 368.

——, ——, and ——, 1995b: On the parameterization of equatorial turbulence: Effect of fine-scale variations below the range of the diurnal cycle. *J. Geophys. Res.,* **100,** 18 333–18 348.

Pritchard, D. W., 1952: Salinity distribution and circulation in the Chesapeake Bay estuarine system. *J. Mar. Res.,* **11,** 106–123.

——, 1954: A study of the salt balance in a coastal plain estuary. *J. Mar. Res.,* **13,** 133–144.

——, 1956: The dynamic structure of a coastal plain estuary. *J. Mar. Res.,* **15,** 33–42.

Regener, M., B. Szilagyi, and H. Baumert, 1997: The generic 1-D turbulence-SPM model. Tech. Rep. 48, 46 pp. [Available from Proudman Oceanographic Laboratory, Bidston Observatory, Birkenhead CH437RA, United Kingdom.]

Rohr, J. J., E. C. Itsweire, K. N. Helland, and C. W. Van Atta, 1988: Growth and decay of turbulence in a stably stratified shear flow. *J. Fluid Mech.,* **195,** 77–111.

Schumann, U., and T. Gerz, 1995: Turbulent mixing in stably stratified shear flows. *J. Appl. Meteor.,* **34,** 33–48.

Simpson, J. H., J. Brown, J. Matthews, and G. Allen, 1990: Tidal straining, density currents, and stirring in the control of estuarine stratification. *Estuaries,* **13,** 125–132.

——, W. R. Crawford, T. P. Rippeth, A. R. Campbell, and J. V. S. Cheok, 1996: The vertical structure of turbulent dissipation in shelf seas. *J. Phys. Oceanogr.,* **26,** 1580–1590.

Taylor, G. I., 1935: Statistical theory of turbulence. Parts I–IV. *Proc. Roy. Soc. London A,* **151,** 421–478.

Thorpe, S. A., 1977: Turbulence and mixing in a Scottish loch. *Philos. Trans. Roy. Soc. London A,* **286,** 125–181.

Trowbridge, J. H., W. R. Geyer, M. M. Bowen, and A. J. Williams III, 1999: Near-bottom turbulence measurements in a partially mixed estuary: Turbulent energy balance, velocity structure, and along-channel momentum balance. *J. Phys. Oceanogr.,* **29,** 3056–3072.

Van Atta, C. W., 1999: On parameterizing turbulence growth rates and fluxes in nonequilibrium stably stratified turbulent shear flows. *J. Mar. Syst.,* **21,** 103–112.